Journal of Nuclear Materials 554 (2021) 153035

Contents lists available at ScienceDirect

Journal of Nuclear Materials

journal homepage: www.elsevier.com/locate/jnucmat

High temperature mechanical properties of fluorite crystal structured materials (CeO_2, ThO_2, and UO_2) and advanced accident tolerant fuels (U_3Si_2, UN, and UB_2)

D. Frazer[a,b,*], B. Maiorov[c], U. Carvajal-Nuñez[a], J. Evans[c,d], E. Kardoulaki[a], J. Dunwoody[a], T.A. Saleh[a], J.T. White[a]

[a] Material Science and Technology Division, Los Alamos National Laboratory, Los Alamos, NM, USA
[b] Advanced characterization and PIE, Idaho National Laboratory, Idaho Falls, ID, USA
[c] MPA, Los Alamos National Laboratory, Los Alamos, NM, USA
[d] Department of Irradiated Fuels and Materials, Idaho National Laboratory, Idaho Falls, ID, USA

ARTICLE INFO

Article history:
Received 16 February 2021
Revised 9 April 2021
Accepted 26 April 2021
Available online 5 May 2021

Keywords:
High temperature nanoindentation
Resonant ultrasound spectroscopy
Accident tolerant fuels
Mechanical properties
Elastic constants

ABSTRACT

The mechanical interaction between the fuel and cladding that occurs during operation of a nuclear reactor is important to understand as it can lead to cladding failures and release of radioactive material into the coolant. In order to develop better models of the pellet-clad mechanical interactions , the mechanical properties of the fuel at relevant operating temperatures, like the elastic moduli, are needed for current and advanced accident tolerant fuels (ATFs). In this work, elevated temperature nanoindentation and resonant ultrasound spectroscopy were used to measure the moduli and hardness of several fluorite materials (CeO_2, ThO_2, UO_2) and several ATF candidates (ATF) (U_3Si_2, UN, UB_2). In addition, a comparison of the two techniques was performed in this study to independently validate the mechanical properties.

1. Introduction

The mechanical properties of established nuclear fuels and potential fuel forms are important for understanding the pellet clad mechanical interactions (PCMI) that occur during operation of a reactor [1,2]. During operation, the cladding material will creep down, and the fuel will swell leading to contact and, therefore, development of stresses between the cladding and the fuel. The PCMI is related to the limited ability of the currently used fuel in light water reactors, uranium dioxide (UO_2), to creep at the current operating temperatures. As a result, stresses increase at the fuel-cladding interface and, along with the buildup of fission products, this promotes stress corrosion cracking in the cladding material. The PCMI can lead to failures in the cladding which leads to ingress of coolant into the cladding rod and egress of solid and gaseous radioactive material into the coolant stream. In order to better understand the phenomenon of PCMI, the mechanical properties of different fuel forms at the operating temperature of the pellet, especially the periphery of the fuel pellets, are needed.

In the literature, the mechanical properties of polycrystalline UO_2 have been evaluated from 25°C to 1700°C [3–23]. This work includes measuring creep in UO_2 at temperatures greater than 1000°C [3–10]. In addition, the mechanical and elastic property measurements have been performed on accident tolerant fuel (ATF) candidates like UN [24–27], U_3Si_2 [28–33] and UB_2 [34–36]. These ATF candidates have desirable properties in comparison to UO_2, such as increased uranium density and higher thermal conductivity [29]. Lastly, there have been limited investigations of the mechanical properties of CeO_2 as a function of temperature [37–40], a surrogate for PuO_2 [39]. There have also been several studies on the mechanical properties of ThO_2 [41–45]. While fresh fuel has low levels of radioactivity and can usually be handled in special laboratory space, spent fuel contains highly radioactive fission products requiring handling in hot cells, which makes the mechanical testing time consuming and costly. Small scale mechanical testing (SSMT) reduces the volume of material needed for mechanical testing which allows for testing outside of hot cells and reduces the cost of post-irradiation examination (PIE) [18].

A variety of experimental techniques can be used to measure the elastic and mechanical properties of nuclear fuels. Two of these techniques are nanoindentation [46,47] and resonant ultrasound spectroscopy (RUS) [48–50]. Both have the advantage of being able

* Corresponding author.
E-mail address: david.frazer@inl.gov (D. Frazer).

https://doi.org/10.1016/j.jnucmat.2021.153035
0022-3115/

Table 1
Measured geometric densities of the materials used in this study when compared to their theoretical density.

Sample	CeO_2	ThO_2	UO_2	U_3Si_2	UN	UB_2
Density (%)	96.54	90.8	95.92	94.73	90.74	91.68

to measure the mechanical or elastic properties over a temperature range. Nanoindentation is a technique that can be used to measure the Young's modulus and hardness of a sample over a temperature range [46,47]. The benefits of nanoindentation include the relatively simple sample preparation, low volume of material needed, and the high temperature conditions that can be reached with these instruments. This is advantageous when working with spent fuel as most of the sample preparation is conducted in hot cells where sample manipulation and handling are difficult.

In this study, elevated temperature nanoindentation was performed on a variety of compounds that include UO_2, CeO_2, ThO_2, U_3Si_2, UN, and UB_2. Elevated temperature RUS is a technique that can be used to determine the elastic constants of a material over a temperature range. RUS was performed on CeO_2, UO_2, and U_3Si_2 for comparison to the nanoindentation results. RUS is a non-destructive, high-precision technique that can evaluate the bulk elastic properties of a material [51]. It is also sensitive to the internal texture of the material [52]. The absolute accuracy of RUS can be much less than 1% with a sensitivity to detect relative variations smaller than 1 part per million [53] allowing for highly accurate measurements of the elastic constants of the material. These characteristics make RUS ideal to explore the temperature dependence of the elastic constants in radioactive materials. Before widespread use of nanoindentation and RUS on spent fuel are implemented, they must be demonstrated and qualified with fresh fuel forms.

2. Experimental

The materials chosen for this study were CeO_2 [39], ThO_2, UO_2 [50], U_3Si_2 [29,32], UN, and UB_2 [35], where the fabrication details are provided in the respective citations. The ThO_2 and UN were sintered using powder metallurgical routes in a glove box with a high purity Ar atmosphere where O_2 was maintained below 20 ppm. The UN was sintered at 2200°C under N_2/H_2 atmosphere to prevent decomposition of UN. UO_2 was chosen because it is the standard fuel in most commercial reactors today. CeO_2 and ThO_2 were evaluated because they have the same crystal structure as UO_2. U_3Si_2, UN, and UB_2 were chosen as they all have been proposed as accident tolerant fuel candidates.

The theoretical densities as calculated from the geometric values of the samples and their masses are shown in Table 1. The samples for nanoindentation were cut approximately 1 mm thick, then they were ground and polished to a 1 μm finish. The samples were then vibrometed for 24 hours in 0.05 µm colloidal silica. The nanoindentation system used for these high temperature indents was a Hysitron TriboIndenter (Bruker Hysitron TriboIndenter, Bruker AXS, Madison, WI, USA) with the XSOL 800 hot stage. In these experiments, a Berkovich cubic boron nitride (cBN) tip was used and calibrated on a fused silica standard. The tip was calibrated on the fused silica standard prior to performing and after completion of the indents on each sample.

The environmental control for high temperature nanoindentation of uranium compounds is extremely important, as they can be reactive with oxygen [54]. The XSOL 800 nanoindentation stage is equipped with a cover gas system to minimize oxidation. However, early studies suggested that additional precautions were required to minimize oxidation in the nanoindenter chamber. This was achieved with additional feedthroughs to allow for the chamber to be purged with an inert or reducing atmosphere in order to inhibit oxidation of the samples. The oxygen in the Triboindenter enclosure was monitored using a GasAlert Extreme Single Gas Detector (BW technologies, Alberta, Canada) with a detection limit of 0.1% (1,000 ppm) oxygen. The GasAlert oxygen sensor was mounted slightly higher in the enclosure than the sample position. The sample chamber was purged overnight until an undetectable quantity of oxygen was measured on the oxygen sensor and was further flushed for an additional 2-3 hours to ensure the sample was in a reduced oxygen atmosphere. Additionally, the gas was run through the XSOL 800 hot stage with its own inlet and outlet supplies.

The high temperature nanoindentation measurements of the , U_3Si_2, UN, and UB_2 samples were performed in argon-rich atmospheres. An argon + 6% H_2 gas mixture was used for the UO_2 and ThO_2 sample. The argon + 6% H_2 gas mixture was not used for the other samples because hydriding has been observed or suspected in the literature [55,56].

For the CeO_2, ThO_2, and UO_2, the nanoindentation experiments were performed at room temperature 298 K (RT), 373 K, 573 K, 773 K, and 973 K. The elevated temperature indents on the U_3Si_2 and UN samples were performed at RT, 373 K, and 473 K, while the indents on the UB_2 sample were performed at RT, 373 K, 473 K, 573 K, and 673 K. As well be discussed later in the manuscript the accident tolerant fuels could not reach higher temperature because of oxidation effects on the surface.

Purging the chamber of the nanoindentation system with inert or reducing environments leads to challenges when using the full load of the indentation head. Utilizing an inert or reducing atmosphere reduced the maximum load of the indenter to 3-4 mN (as compared with ~ 18 mN in air), and produced anomalous displacement events in the load-versus-displacement curves in higher loading conditions. The maximum temperature reached with the more air sensitive compounds was lower than the maximum testing temperature because of oxide formation on the samples surface. This oxide formation can be seen with the U_3Si_2, UN, and UB_2 compounds. No changes in the sample surfaces were observed after the measurements for thefluorite crystal structured materials during nanoindentation.

All of the samples were heated at 20°C min^{-1} to the desired testing temperatures and were allowed to thermally equilibrate for 10 minutes at each desired testing temperature for the nanoindentation experiments. The cBN tip on the TriboIndenter is not actively heated which can lead to thermal drift during the measurement. To minimize thermal drift during the nanoindentation, the tip was placed in contact with the sample for 5 minutes to equilibrate with the sample temperature. After heating the tip, indentations were performed on the sample at the desired testing temperature. At each test temperature, on each sample 16 individual indents with a spacing of at least 20 µm, were collected for statistical averaging of random grain orientations. Optical inspection of the grid of indents was performed using the indenter's microscope. Indents performed on or near pores were removed from the data set. The removal of these indents would leave indents performed far from pores enabling the probing of nearly fully dense material. The Young's modulus was calculated from the reduced modulus measure with nanoindentation system using Eq. (1).

$$\frac{1}{E_r} = \frac{\left(1-\nu_s^2\right)}{E_s} + \frac{\left(1-\nu_i^2\right)}{E_i} \quad (1)$$

where E_r is the reduced modulus measured with the indenter, E_s is the elastic modulus of the sample, ν_s is the Poisson's ratio for the samples, E_i is the elastic modulus for the indenter (680 GPa), ν_i is the Poisson's ratio for the indenter (0.15). In Eq. (1), the value for elastic modulus of cBN tip, E_i, is corrected for the temperature of the test using the equation in [57]. The following Poisson's ratios for the samples were used 0.185 for U_3Si_2 [29,32], 0.28 for UN [26],

0.1 for UB_2 [35] 0.3 for UO_2 [23,30], 0.3 for CeO_2 [38–40], and 0.3 for ThO_2 [41–45].

The samples for RUS were sintered and cut into 5 × 5 mm right cylinders. High temperature RUS measurements were performed using a probe that was fabricated in-house as described elsewhere [53]. The RUS measurements of the CeO_2, UO_2, and U_3Si_2 samples were performed from RT to 500 K in an atmosphere of low pressure, ultra-high purity He atmosphere. The sample space was evacuated to 10^{-6} torr and refilled several times to remove oxygen from the atmosphere. No changes in the sample surfaces were observed after the measurements of the samples in the high temperature RUS experiments. The sample was held with minimal pressure (<5g) between two $LiNbO_3$ transducers, one of which provides excitation of a sinusoidal function of frequency f while the other continuously measures the displacement produced in the sample. All the wiring and connections were made to withstand elevated temperatures [53]. The software and electronics used to obtain and analyze the resonances are described elsewhere [51]. The temperature ramp rate was 0.1-0.2 K•min^{-1}. Since it takes about one minute to obtain a satisfactory resonance spectrum, this represents a full elastic tensor data set every 0.1 K. Increasing and decreasing temperature measurements show no visible hysteresis, indicating very good thermal agreement between the thermometer and the samples and no irreversible behavior in the samples.

The elastic constants of the pellets were obtained from the resonance spectra using the Rayleigh Ritz inversion method, as described in the literature [48,49,58]. The prediction of the resonance frequencies are evaluated from the sample density, sample geometry, and initial guesses for the elastic constants. The predicted frequencies are then compared with the experimental values and are iteratively refined by varying the elastic constants to obtain fitting errors below an acceptable level. At least 40 resonance peaks for each sample were obtained and indexed. The associated uncertainties (as defined by the difference between the predicted and experimentally indexed resonance frequencies) for UO_2, CeO_2, and U_3Si_2 were 0.32%, 0.27% and 0.41%, respectively. These samples were assumed to be polycrystalline and isotropic, as is expected for these unirradiated materials produced by conventional pressing and sintering of powders. Using Voigt notation, isotropic materials are associated with only two independent elastic constants, C_{11} (the compressive elastic constant) and C_{44} (the shear elastic constant), whereby the dilatational elastic constant is defined by $C_{12} = C_{11} - 2C_{44}$. The C_{11} and C_{44} elastic constants obtained with RUS can be used to calculate the elastic moduli and Poisson's ratio of the specimens, where other properties such as shear modulus ($G = C_{44}$), bulk modulus (K), Young's modulus or Young's modulus (E), and Poisson's ratio are given in Eqs. (2)–(4).

$$K = C_{11} - \frac{4}{3}C_{44} \tag{2}$$

$$E = 3K(1 - 2\nu) = 2G(1 + \nu) \tag{3}$$

$$\nu = \frac{C_{11} - 2C_{44}}{2(C_{11} - C_{44})} \tag{4}$$

3. Results and discussion

The results for the Young's modulus obtained from nanoindentation for the fluorite materials which are CeO_2, ThO_2, and UO_2 as a function of temperature are shown in Fig. 1A–C. It can be seen that the Young's modulus for all of the fluorite materials decreases with temperature in a linear manner. This is seen in other oxide materials [59] and fits with the Varshni theory [60]. For the CeO_2 values in Fig. 1A it can be seen that our Young's modulus at room temperature matches well with both experimental and modeled literature values [38,39]. No elevated temperature Young's modulus data was found in the literature for CeO_2. In addition, the mass of the fluorite samples was measured before and after the elevated temperature nanoindentation and no change in mass was detected. The Young's modulus of ThO_2 measured with nanoindentation over temperature (Fig. 1B) also agrees well with literature values [43,44]. In addition the values for UO_2 (Fig. 1C), agree well when compared to values from experimental [23] and modeling data [19].

Table 2
The intrinsic hardness and softening coefficients of the fluorite oxide materials.

Sample	CeO_2	ThO_2	UO_2
Intrinsic Hardness [GPa]	15.76	23.81	17.93
Softening Coefficient [K^{-1}]	-0.0025	-0.0026	-0.0026

The hardness values for the fluorite materials are shown in Fig. 2A–C. The data from this study (in red) decrease exponentially with temperature. In Fig. 2A, the nanoindentation hardness of CeO_2 is measured over temperature. The nanoindentation values in [40] agree with our room temperature nanoindentation value within the 9.5% error. In addition, the converted (VH → GPa) Vickers hardness values are 24% lower than those obtained using nanoindentation. The reason for this discrepancy can be attributed to indentation size effects, which are understood to contribute to discrepancies when comparing multiple length scale datasets [61]. Because of the large difference in indentation size and the indentation size effect phenomenon direct comparison of the converted Vickers and nanoindentation values is not advised. However, comparing the nanoindentation and Vickers results is useful to see trends in the hardness behavior of the different materials over temperature. The porosity of the samples measured with Vicker's are unknown, but are usually in the 94-96% of theoretical density range. Due to the limited volume probed during the nanoindentation tests, it is expected that the nanoindentation is measuring closer to 100% dense material property values, which also contributes to the apparent differences between Vicker's hardness and nano-hardness.

Temperature-dependent measured and literature hardness values for ThO_2 are shown in Fig. 2B. The data from [42] was obtained using nanoindentation, and the Young's modulus of ThO_2 using different fabrication routes, which agree well with the values measured here. The hardness data from [41] are converted Vicker's hardness values on polycrystalline ThO_2. Fig. 2C displays the nanoindentation hardness values of UO_2 over temperature compared with literature values [23,41,62]. As shown in Fig. 2, hardness values measured in this study agree (within uncertainty) with other nanoindentation studies [23].

Fig. 2 shows that the hardness decreases exponentially with increasing temperature. This matches well with the predicted behavior from literature [63–66] and can be fitted with Eq. (5):

$$H = Ae^{BT} \tag{5}$$

where H is the hardness, A and B are constants, and T is the temperature in Kelvin. In Eq. (4), A is the intrinsic hardness of the material at $T = 0$ K, and B is the thermal softening coefficient. Plotting the natural logarithm of the hardness values versus T exhibits a linear behavior as shown in Fig. 3. Table 2 shows that all of the fluorite crystal structure materials have nearly identical thermal softening coefficients but different intrinsic hardness values which is expected. The values for the intrinsic hardness and thermal softening coefficients measured on UO_2 here match well with those from literature [23].

In Fig. 4A–C we present the Young's moduli versus temperature for the ATF candidates such as U_3Si_2, UN, and UB_2. Fig. 4A–C

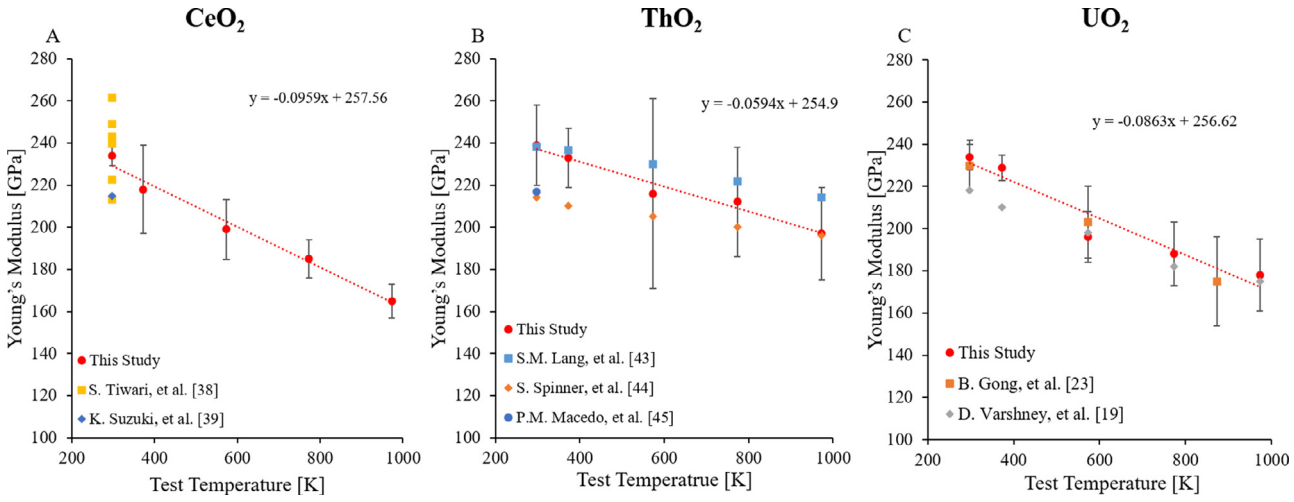

Fig. 1. The Young's modulus of (A) CeO_2, (B) ThO_2, and (C) UO_2 the oxide fluorite structure material over testing temperature as measured using nanoindentation. At each test temperature on each sample a minimum of 16 indents was performed with a 20 μm spacing.

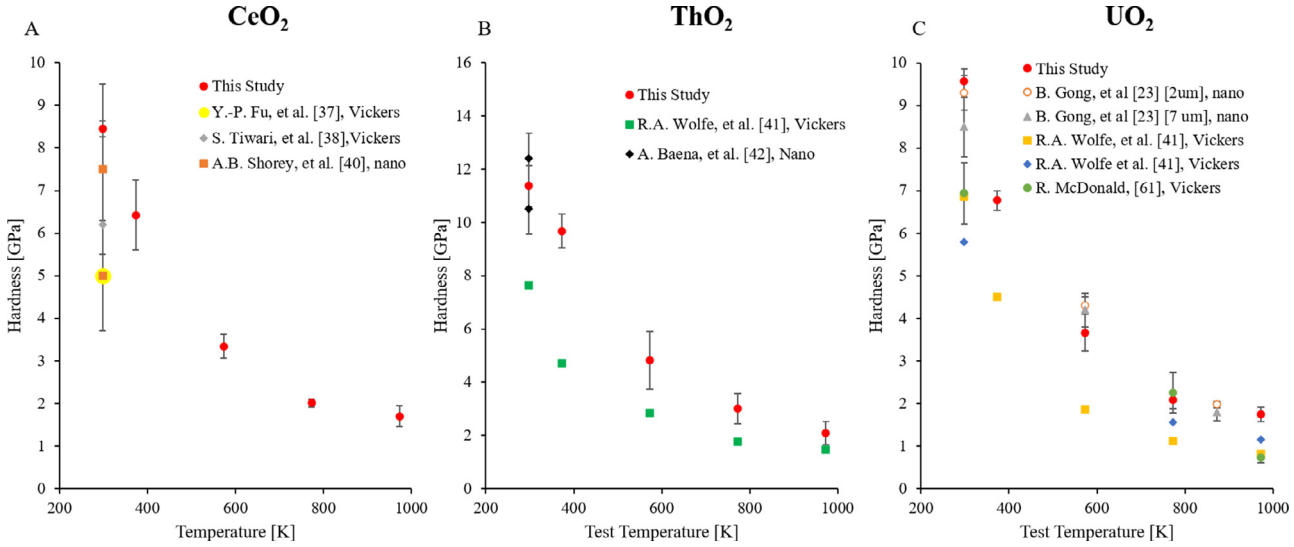

Fig. 2. The nanoindentation hardness of the oxide fluorite structure materials over testing temperature. At each test temperature on each sample a minimum of 16 indents was performed with a 20 μm spacing. (A) CeO_2, (B) ThO_2 and (C) UO_2.

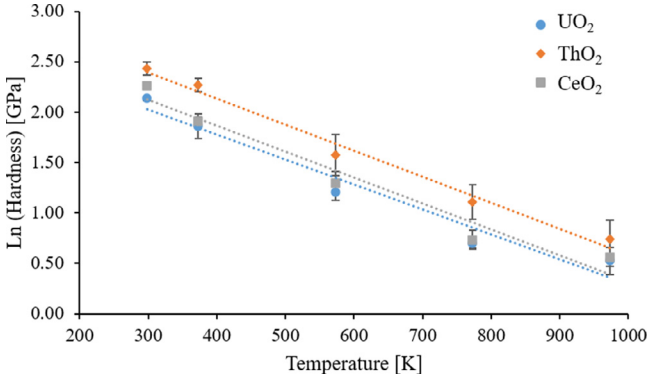

Fig. 3. The ln(Hardness) versus temperature for the three fluorite crystal structure materials.

shows that there is significantly less data available in literature for comparison with these materials. This study illustrates the advantage of nanoindentation at the laboratory scale to quickly evaluate mechanical properties. It can be seen in Fig. 4A that the Young's modulus value measured for U_3Si_2 in this study (in red) agree with available literature within error [32]. The same agreement is evident in Fig. 4B for UN [25,26]. For the case of UB_2 there was room temperature data [35,67,68] for comparison purposes. In [67,68] the elastic modulus came from simulation work while the values here come from experimental work which could reason for the large difference in values.

In Fig. 5A–C the temperature-dependent hardness of the ATF candidates. Again, experimental data from literature is extremely limited for comparison. From Fig. 5A, the U_3Si_2 nanoindentation hardness measured in this work agrees (within uncertainty) to the nanoindentation value found in literature [32]. As shown in Fig. 5B the same trend is observed that the nanoindentation values are higher than the Vickers hardness values for UN. The U_3Si_2 and UB_2 both have higher hardness than UO_2, the current fuel of LWRs today. The UN has similar hardness value to UO_2 over the tested temperature range.

The nanoindentation temperature range for the ATF (673 K) was lower than that of the fluorite materials tests (973 K), (see Figs. 1 and Figure 4). As stated earlier the environmental control for testing these uranium compounds is essential [52]. The sur-

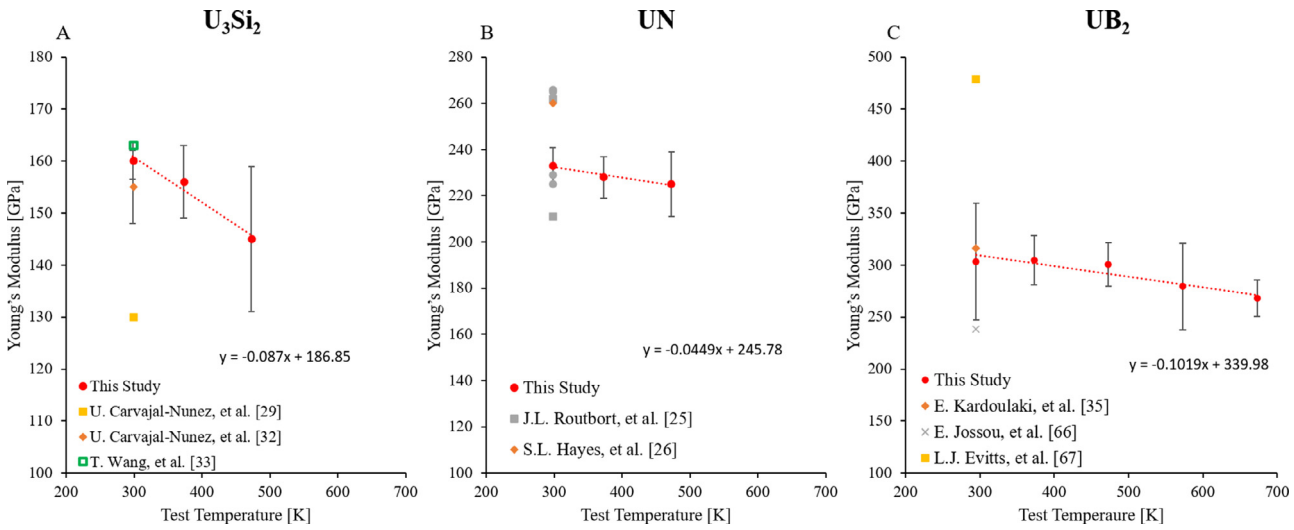

Fig. 4. The Young's modulus of the advanced ATF over temperature as measured using nanoindentation. At each test temperature on each sample a minimum of 16 indents was performed with a 20 μm spacing. (A) U_3Si_2, (B) UN, and (C) UB_2.

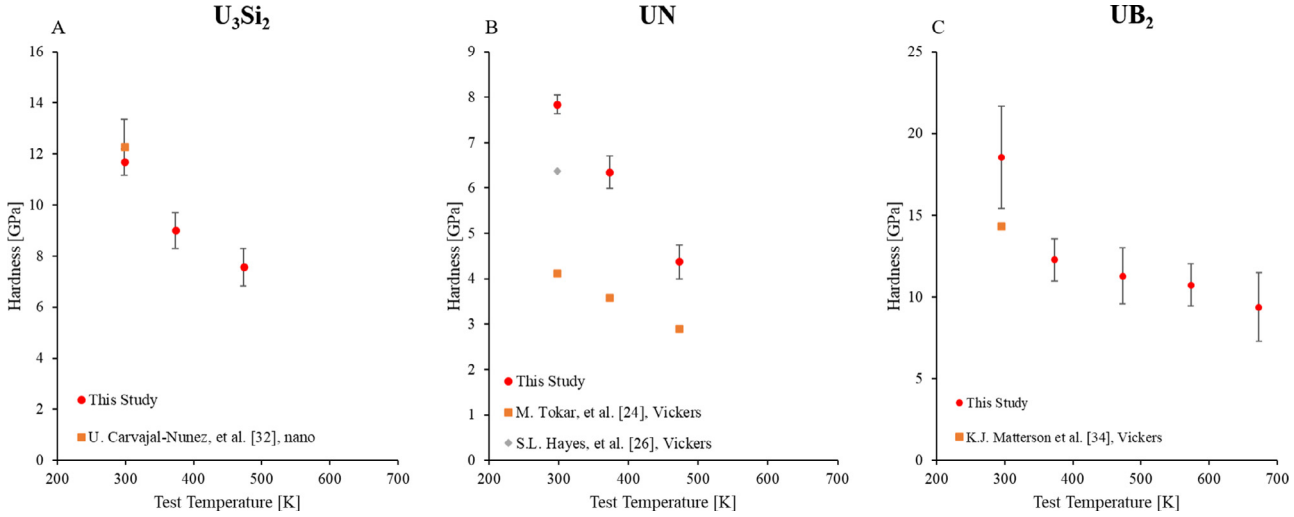

Fig. 5. The temperature-dependent nanoindentation hardness of the ATF candidates. At each test temperature on each sample a minimum of 16 indents was performed with a 20 μm spacing. (A) U_3Si_2, (B) UN, and (C) UB_2.

faces of the U_3Si_2 and UN samples before the nanoindentation experiments and after reaching temperature are shown in Fig. 6. We measured up to 473 K (U_3Si_2 and UN) and 673 K (UB_2) where we had to stop to preserve the samples integrity. Our measurements indicate that UB_2 is less sensitive to oxidation compared to U_3Si_2 and UN. However, further investigation is required to confirm this assertion. In addition, to confirm that these surface interactions did not affect the results the samples were re-polished sufficiently to remove these features. The indentation was performed again with the surface of the sample being evaluated with attached optical microscope after each temperature step to ensure there was no visible change in the sample surface.

In Fig. 7 the hardness and thermal softening coefficients for the ATF candidates are shown. In Table 3 it is observed that UB_2 has the lowest thermal softening coefficient while UN has the highest. Note (from Fig. 5) that the room temperature value of ln(hardness) value for UB_2 is associated with higher uncertainty, which might be artificially increasing the slope of the ln(hardness) vs. temperature curve shown in Fig. 7. If the UB_2 ln(hardness) room temperature outlier is removed, then this results in a softening coefficient of -0.0009. The softening coefficient for U_3Si_2 is similar to that of

Table 3
The intrinsic hardness and softening coefficients of the ATF candidates.

Sample	U_3Si_2	UN	UB_2
Intrinsic Hardness [GPa]	23.16	21.11	25.14
Softening Coefficient [K^{-1}]	-0.0024	-0.0033	-0.0015

fluorite materials, as shown in Table 2. It should be noted that the fluorite materials were evaluated at higher temperatures than the ATFs, but this data shows that the ATF candidates have higher intrinsic hardness than CeO_2 and UO_2.

The Young's modulus and hardness for UN and UO_2 are similar at room temperature. U_3Si_2 has a lower Young's modulus and higher hardness at room temperature as compared with UO_2. Lastly, UB_2 has both a higher hardness and Young's modulus value at room temperature. In most commercial light water reactors, the periphery of the pellet during operation is operating at around 773 K (500°C). As we were not able to reach those temperature for the ATFs, we extrapolated their hardness values to that temperature using Eq. (4). The calculated hardness at 773 K for the materials of

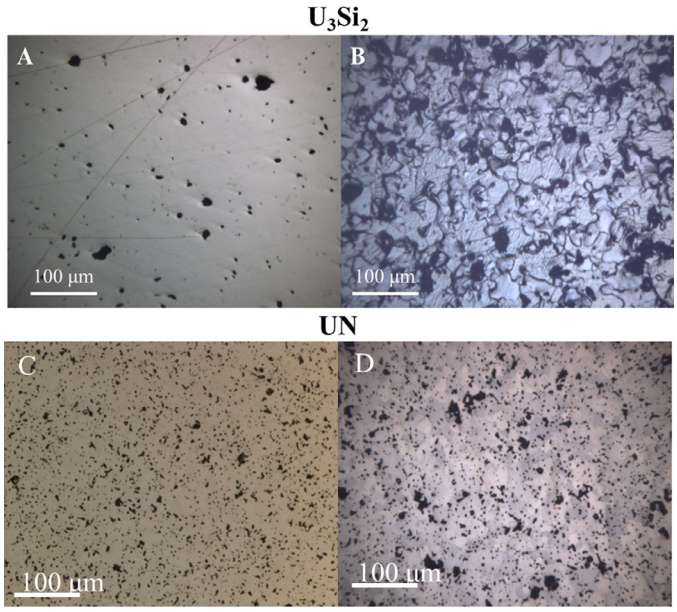

Fig. 6. (A) The surface of the U_3Si_2 sample before testing in the nanoindenter. (B) The surface of the U_3Si_2 sample after reaching 473 K in the nanoindenter. (C) The surface of the UN sample before testing in the nanoindenter. (D) The surface of the UN sample after reaching 473 K in the nanoindenter.

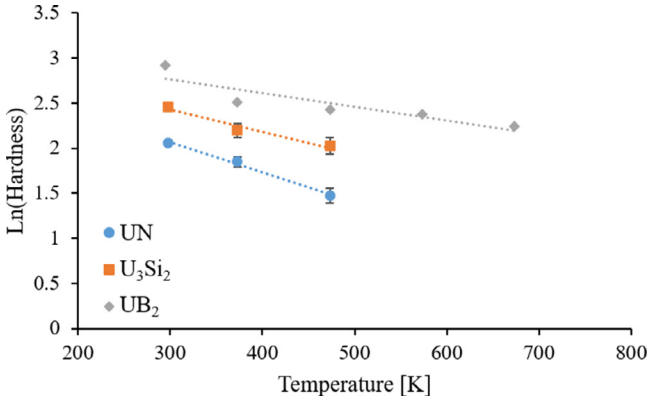

Fig. 7. The ln(Hardness) versus temperature for the UN, U_3Si_2, and UB_2.

interest are: UO_2 = 2.1 GPa (measured), U_3Si_2 = 3.6 GPa, UN = 1.7 GPa, and UB_2 = 7.9 GPa. As a reminder, this is a comparison of the fresh fuel properties and will change as irradiation damage accumulates. At 773 K, only UN has a lower hardness than UO_2, while both U_3Si_2 and UB_2 have higher values. The UB_2 hardness value is nearly 4 times that of the UO_2 value which could cause challenges with PCMI during operation. The UB_2 could deform less than UO_2 which could increase the possibility for stress corrosion cracking in the cladding material. The same could be said for the U_3Si_2 as well but to a lesser extent.

The H/E ratio characterizes the resistance of the material to elastic deformation, while the H^3/E^2 ratio provides an estimate of the material's ability to dissipate energy as plastic deformation during loading. The H^3/E^2 ratio also shows that the contact loads needed to induce plasticity are higher in materials with a larger value [69]. The H/E and H^3/E^2 values are tabulated in Table 4 for room temperature and for 773 K (extrapolated values). The H^3/E^2 for U_3Si_2 and UB_2 are an order of magnitude larger than for UO_2 at 773 K. This suggests that these two ATF candidates would require significantly larger loads than UO_2 to induce plasticity in fuel which could challenges for mitigating the PCMI.

Table 4
The $H{\bullet}E^{-1}$ and $H^3{\bullet}E^{-2}$ ratios for UO_2 and the ATF fuels at RT and 773 K.

Material	Temperature	$H{\bullet}E^{-1}$	$H^3{\bullet}E^{-2}$
UO_2	RT	0.0409	0.0160
	773 K	0.0112	0.0003
U_3Si_2	RT	0.0717	0.0601
	773 K	0.0302	0.0033
UN	RT	0.0342	0.0092
	773 K	0.0078	0.0001
UB_2	RT	0.0612	0.0694
	773 K	0.0302	0.0072

The elastic properties measured (C_{11} and C_{44}) from 295 K to 500 K using RUS can be seen in Fig. 8. The high precision of the RUS measurements allows observation of the small deviation from the linear expected behavior at these temperatures. It can be observed that the CeO_2 sample behaves according to a predicted Varshni dependence [60]. The UO_2 and U_3Si_2 samples behave differently, in particular the shear modulus (C_{44}) for UO_2 and compression modulus (C_{11}) in U_3Si_2. In the case of UO_2, this behavior is due to the paramagnetic/antiferromagnetic phase transition at T=30K that causes an anomalously extended softening of shear elastic constant c_{44} up to ambient temperature [70]. For the U_3Si_2, this is not attributed to a spurious factor such as surface degradation (which should have also affected c_{44}), as the sample showed no hysteresis in the temperature behavior nor depicted any visual change in the surface. This anomalous curvature deserves further investigation in future studies.

Fig. 9 illustrates the comparison between the nanoindentation and RUS measurement results for the (A) CeO_2, (B) UO_2, and (C) U_3Si_2. The Young's moduli obtained using RUS are consistently lower than those obtained using nanoindentation for all the materials tested. This is consistent with previous room temperature measurements on U_3Si_2 by Carvajal-Nuñez [29,32] where RUS and nanoindentation measured a Young's modulus of ~130 GPa and 160 GPa, respectively. This is believed to be due, in part, to the relative length scales that both techniques are measuring: RUS measures the entire sample (bulk property) which includes porosity, while nanoindentation is sampling a small volume of highly dense material. While grain orientation influences the nanoindentation results, we performed 16 measurements at each temperature with a large spacing. This should provide for a random assortment of grains to be measured which enables measuring the average property value. Bulk scale RUS measurements would be expected to measure a lower value as porosity lowers the Young's modulus [29,32]. It can however be seen that the difference between the nanoindentation and RUS values decreases with increasing temperature. This could be attributed to a larger plastic volume under the tip, due to deeper indents at higher temperature, so the porosity of the sample has a larger effect on the nanoindentation values measured. This is a different process than the indentation size effect as nanoindentation is measuring accurate Young's modulus values even at shallow depths.

The difference between room temperature Young's modulus as measured by nanoindentation and RUS for CeO_2, UO_2 and U_3Si_2 is 16%, 12%, and 21%, respectively. The porosity for the CeO_2, UO_2, and U_3Si_2 pellets was 3.46%, 4.08%, and 5.27% respectively. The effect of porosity on the Young's modulus can be taken into account using Eq. (6) [71],

$$E = E_0(1-P)/\left\{1 + \frac{(1+\nu_0)(13-15\nu_0)P}{[2(7-5\nu_0)]}\right\} \quad (6)$$

where E is the effective Young's modulus, E_0 is the fully dense Young's modulus, P is the porosity (in units of volume fraction) in the material, and ν_0 is the Poission's ratio of the material. The

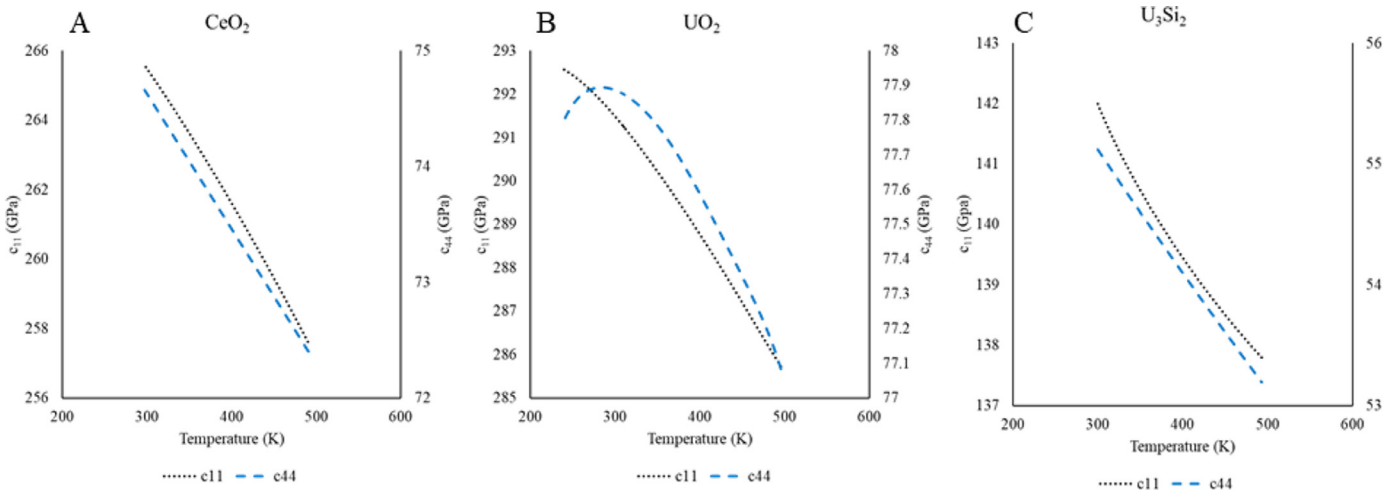

Fig. 8. The temperature-dependent elastic constants of (A) CeO_2, (B) UO_2, and (C) U_3Si_2 as measured using RUS.

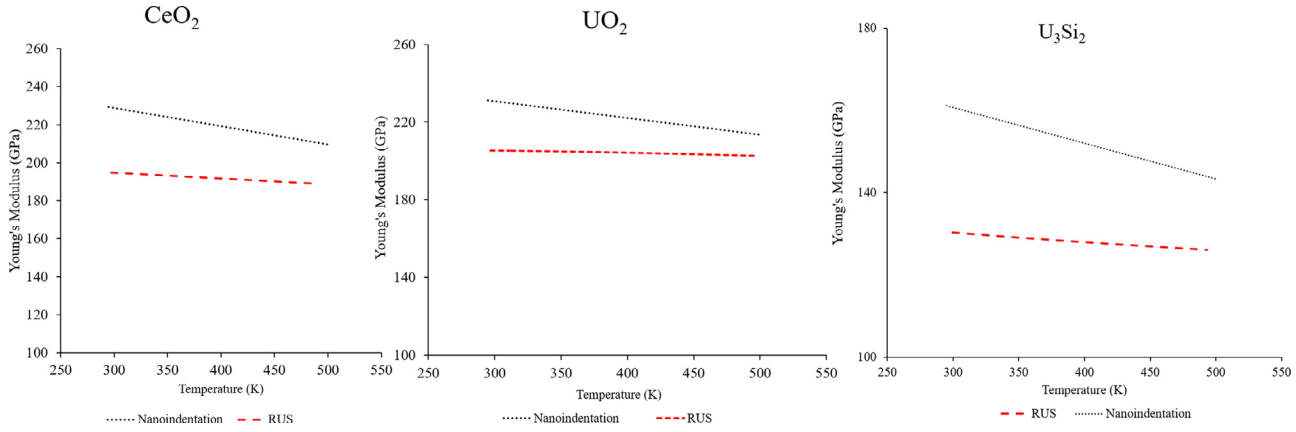

Fig. 9. (A) The temperature-dependent Young's moduli measured using nanoindentation and RUS of (A) CeO_2, (B) UO_2, and (C) U_3Si_2. The Young's moduli for the nanoindentation is a fit of the data.

Table 5
The Young's modulus measured at RT with nanoindentation, RUS, and the nanoindentation corrected for porosity using Eq. (5).

	Nanoindentation [GPa]	Corrected nanoindentation [GPa]	RUS [GPa]	E_0 of RUS [GPa]
CeO_2	229	213	195	209
UO_2	231	212	205	223
U_3Si_2	160	144	130	145

Poission's ratio for the materials were the following 0.185 for U_3Si_2 [29,32], 0.3 for UO_2 [23,30], and 0.3 for CeO_2 [38–40] which should change little over this temperature range. If E_0 is assumed to be the value measured using nanoindentation, we can compare E (calculated from nanoindentation) to E from RUS by accounting for porosity using Eqn 6). Using this approach, the difference in the adjusted nanoindentation and RUS Young's moduli at room temperature for CeO_2, UO_2, and U_3Si_2 are 9%, 3%, and 10% respectively. In addition in evaluating the multi-length scale experiments, the porosity and the Young's modulus values measured with RUS were used to calculate E_0 values using Eq. (6) to compare with nanoindentation values. Those values can be seen in Table 5 in the column labeled "E_0 of RUS". This approach gives a difference in the "E_0 of RUS" and nanoindentation of 9 %, 3% and 9 % for the CeO_2, UO_2 and U_3Si_2 respectively. The good agreement in the Young's modulus between the two length scale techniques can provide avenues for the development of multi-length scale models of materials."

Lastly, in comparing the nanoindentation and RUS to modeling calculations and fits it can be seen in Fig. 10 there is excellent agreement between nanoindentation and RUS results on UO_2 and the MATPRO correlations when corrected for density (in the MATPRO software). The good agreement further validates the RUS and nanoindentation data that was collected for UO_2 and other compounds. The results from the other ATF candidates could be used in codes like MATPRO to assist in enabling predictions of their performance under nuclear reactor operation.

4. Summary and conclusions

In this study, elevated temperature nanoindentation and RUS have provided the mechanical properties of nuclear fuels to increase the knowledge in the community and support modeling efforts of the PCMI during nuclear reactor operation. Nanoindentation provides a capability in the nuclear materials community to measure the Young's modulus and hardness of materials with minimal sample preparation and on small volumes of material.

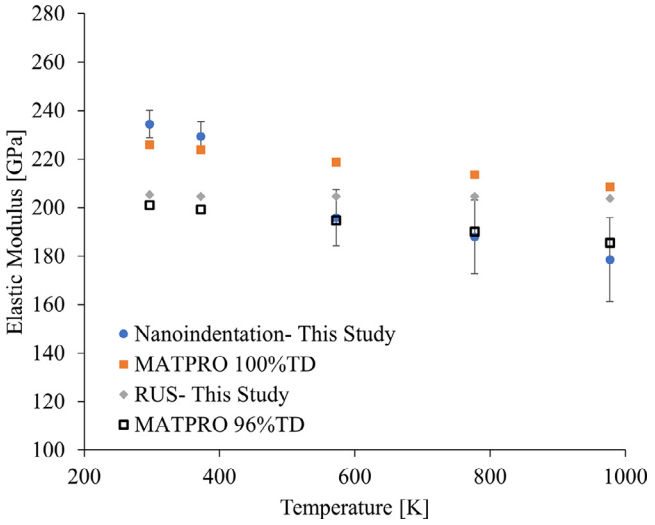

Fig. 10. Young's modulus vs. temperature as determined by nanoindentation, RUS, and MATPRO correlations corrected for density for UO_2.

Nanoindentation can be used to measure these mechanical properties of a wide range of compounds at varying temperatures. Due to the small volumes sampled during testing, this technique can be applied to irradiated fuel in the future at varying temperatures to measure the material's mechanical properties. This study shows that if the Young's modulus measured with nanoindentation is corrected for the bulk porosity of the sample, then the value measured agrees well with those obtained from bulk measurement techniques like RUS. Here, the bulk technique of elevated temperature, RUS, was used as a comparison to nanoindentation. The Young's moduli as determined by RUS and porosity-corrected nanoindentation agree within error. Both techniques have been used to accurately measure the moduli of the materials over a temperature range. Both techniques showed the expected linear decreases in Young's moduli over this temperature range. The environmental control can be a significant challenge when performing elevated temperature measurements of uranium-bearing compounds. The measured nanoindentation and RUS Young's moduli for U_3Si_2 and UB_2 have significantly higher H^3/E^2 values as compared with UO_2 at 773 K. This suggests the possibility that these ATF candidates would need higher contact loads to cause plastic deformation in the fuel, which could exacerbate PCMI. The UN has a lower H^3/E^2 than UO_2, which suggests the possibility that UN might have improved resistance to PCMI during operation.

Declaration of Competing Interest

The authors declare that they have no known competing financial interests or personal relationships that could have appeared to influence the work reported in this paper.

CRediT authorship contribution statement

D. Frazer: Conceptualization, Investigation, Writing – original draft, Visualization. **B. Maiorov:** Investigation, Writing – review & editing, Funding acquisition. **U. Carvajal-Nuñez:** Investigation. **J. Evans:** Investigation, Writing – review & editing. **E. Kardoulaki:** Investigation, Writing – review & editing. **J. Dunwoody:** Investigation, Writing – review & editing. **T.A. Saleh:** Investigation, Funding acquisition. **J.T. White:** Investigation, Writing – review & editing, Funding acquisition.

Acknowledgment

The support of the U.S. Department of Energy, Office of Nuclear Energy Nuclear Technology Research and Development program is gratefully acknowledged. D. Frazer acknowledges the support of the Seaborg Institute through a LANL Seaborg postdoctoral fellowship. Work done by BM was supported as part of the Materials Science of Actinides, an Energy Frontier Research Center funded by the U.S. Department of Energy, Office of Science, Basic Energy Sciences under Award No. DE-SC0001089. This work was per- formed at Los Alamos National Laboratory which is operated by Triad National Security, LLC, for the National Nuclear Security Administration of the U.S. Department of Energy under contract number 89233218CNA0 0 0 0 01.

References

[1] Y.R. Rashid, Mathematical modeling and analysis of fuel rods, Nucl. Eng. Des. 29 (1974) 22–32.
[2] M.C. Billone, R.O. Montgomery, Y.R. Radhid, J.L. Head, Advancements in the behavioral modeling of fuel elements and related structures, Nucl. Eng. Des. 134 (1992) 23–36.
[3] X. Iltis, N. Gey, C. Cagna, A. Hazotte, P. Sornay, Microstructural evolution of uranium dioxide following compression creep tests: an EBSD and image analysis study, J. Nucl. Mater. 456 (2015) 426–435.
[4] X. Iltis, M.B. Saada, H. Mansour, N. Gey, A. Hazotte, N. Maloufi, A new characterization approach for studying relationships between microstructure and creep damage mechanisms of uranium dioxide, J. Nucl. Mater. 474 (2016) 1–7.
[5] M.S. Seltzer, A.H. Clauer, B.A. Wilcox, The influence of stoichiometry on compression creep of polycrystalline UO_{2+x}, J. Nucl. Mater. 44 (1972) 331–336.
[6] M.S. Seltzer, A.H. Clauer, B.A. Wilcox, The influence of stoichiometry on compression creep of uranium dioxide single crystals, J. Nucl. Mater. 44 (1972) 43–56.
[7] W.M. Armstrong, A.G. Causey, W.R. Sturrock, Creep of single-crystal UO_2, J. Nucl. Mater. 19 (1966) 42–49.
[8] F. Dherbey, F. Louchet, A. Mocellin, S. Leclercq, Elevated temperature creep of polycrystalline uranium dioxide: from microscopic mechanisms to macroscopic behavior, Acta Materialia 50 (2002) 1495–1505.
[9] M. Salvo, J. Sercombe, J.C. Menard, J. Julien, T. Helfer, T. Desoyer, Experimental characterization and modelling of UO_2 behavior at high temperature and high strain rates, J. Nucl. Mater. 456 (2015) 54–67.
[10] O.A. Ruano, J. Wolfenstine, J. Wadsworth, O.D. Sherby, Harper-Dorn and power law creep in Uranium dioxide, Acta Metall. Mater. 39 (1991) 661–668.
[11] J.F. Byron, Yield and flow of polycrystalline uranium dioxide, J. Nucl. Mater. 27 (1968) 48–53.
[12] R.J. Keller, T.E. Mitchell, A.H. Heuer, Plastic deformation in nonstoichiometric UO_{2+x} single crystals—1. Deformation at low temperatures, Acta Metall. 36 (1988) 1061–1071.
[13] K.C. Radford, G.R. Terwilliger, Compressive Deformation of Polycrystalline UO_2, J. Am. Ceram. Soc. 58 (1975) 274–278.
[14] A.G. Evans, R.W. Davidge, The strength and fracture of stoichiometric polycrystalline UO_2, J. Nucl. Mater. 33 (1969) 249–260.
[15] R.F. Canon, J.T.A. Roberts, R.J. Beals, Deformation of UO_2 at High Temperatures, J. Am. Ceram. Soc. 54 (1971) 105–112.
[16] D. Frazer, B. Shaffer, K. Roney, H. Lim, B. Gong, P. Peralta, P. Hosemann, Small--scale mechanical testing of UO_2, Trans. Am. Nucl. Soc. 116 (2017) 485–487.
[17] D. Frazer, B. Shaffer, K. Roney, H. Lim, B. Gong, P. Peralta, P. Hosemann, Elevated temperature nanoindentation testing of UO_2, Trans. Am. Nucl. Soc. 117 (2017) 623–624.
[18] K.A. Terrani, M. Balooch, J.R. Burns, Q.B. Smith, Young's modulus evaluation of high burnup structure in UO_2 with nanometer resolution, J. Nucl. Mater. 508 (2018) 33–39.
[19] D. Varshney, S. Shtiya, Pressure and temperature dependent elastic, mechanical and thermodynamical properties of nuclear fuel: UO_2 and UN_2, J. Nucl. Mater. 440 (2013) 344–365.
[20] L. Portelette, J. Amodeo, R. Madec, J. Soulacroix, T. Helfer, B. Michel, Crystal viscoplastic modeling of UO_2 single crystal, J. Nucl. Mater. 510 (2018) 635–643.
[21] A.V. Lunev, A.Y. Kuksin, S.V. Starikov, Glide Mobility of the ½[110](001) edge dislocation in UO_2 from molecular dynamics simulation, Int. J. Plast. 89 (2017) 85–95.
[22] D. Frazer, P. Hosemann, Plasticity of UO_2 quantified and understood via elevated temperature micro compression testing, J. Nucl. Mater. 525 (2019) 140–144.
[23] B. Gong, D. Frazer, T. Yao, P. Hosemann, M. Tonks, J. Lian, Nano- and Micro-indentation testing of sintered UO_2 fuel pellets with controlled microstructure and stoichiometry, J. Nucl. Mater. 516 (2019) 169–177.
[24] M. Tokar, A.W. Nutt, J.A. Leary "Mechanical properties of carbide and nitride reactor fuels"
[25] J.L. Routbort, R.N. Singh, Elastic, diffusional, and mechanical properties of carbide and nitride nuclear fuels – a review, J. Nucl. Mater. 58 (1975) 78–114.

[26] S.L. Hayes, J.K. Thomas, K.L. Peddicord, Material property correlations for uranium mononitride: II. Mechanical properties, J. Nucl. Mater. 171 (1990) 271–288.

[27] J. Adachi, K. Kurosaki, M. Uno, S. Yamanaka, M. Takano, M. Akabori, K. Minato, Mechanical properties at sub-microscale and macroscale of polycrystalline uranium mononitride, J. Nucl. Mater. 384 (2009) 6–11.

[28] B. Gong, T. Yao, P Lei. J. Harp, A.T. Nelson, J. Lian, Spark plasma sintering (SPS) densified U_3Si_2 pellets: Microstructure control and enhanced mechanical and oxidation properties" J, All. Comp. 825 (2020) 154022.

[29] U. Carvajal-Nunez, T.A. Saleh, J.T. White, B. Maiorov, A.T. Nelson, Determination of elastic properties of polycrystalline U_3Si_2 using resonant ultrasound spectroscopy, J. Nucl. Mater. (2017), doi:10.1016/j.jnucmat.2017.11.008.

[30] K.E. Metzger, T.W. Knight, E. Roberts, X. Huang, Determination of mechanical behavior of U_3Si_2 nuclear fuel by microindentation method, Prog. Nucl. Energy 99 (2017) 147–154.

[31] A. Mohamad, Y. Ohishi, H. Muta, K. Kurosaki, S. Yamanaka, Thermal and mechanical properties of polycrystalline U_3Si_2 synthesized by spark plasma sintering, J. Nucl. Sci Tech. 55 (2018) 1144–1150.

[32] U. Carvajal-Nunez, M.S. Elbakhshwan, N.A. Mara, J.T. White, A.T. Nelson, Mechanical properties of uranium silicides by nanoindentation and finite elements modeling, JOM 70 (2018) 203–208.

[33] T. Wang, N. Qiu, X. Wen, Y. Tian, J. He, K. Luo, X. Zha, Y. Zhou, Q. Huang, J. Lang, S. Du, First-principles investigations on the electronic structures of U_3Si_2, J. Nucl. Mater. 469 (2016) 194–199.

[34] K.J. Matterson, H. Jones, A study of the tetraborides of uranium and thorium, Trans. Br. Ceram. Soc. 60 (1961) 475–493.

[35] E. Kardoulaki, J.T. White, D.D. Byler, D.M. Frazer, A.P. Shivprasad, T.A. Saleh, B. Gong, T. Yao, J. Lian, K.J. McClellan, Thermophysical and mechanical property assessment of UB_2 and UB_4 sintered via spark plasma sintering, J. All. Compd. 818 (2020) 153216.

[36] E. Kardoulaki, D.M. Frazer, J.T. White, U. Carvajal, A.T. Nelson, D.D. Byler, T.A. Saleh, B. Gong, T. Yao, J. Lian, K.J. McClellan, Fabrication and thermophysical properties of UO_2-UB_2 and UO_2-UB_4 composites sintered via spark plasma sintering, J. Nucl. Mater. 544 (2020) 152690.

[37] Y.-P. Fu, S.-H. Hu, B.-L. Liu, Structure and characterization and mechanical properties of CeO_2-ZrO_2 solid solution system, Ceram. Inter. 35 (2009) 3005–3011.

[38] S. Tiwari, N. Balasubramanian, S. Biring, S. Sen, Effect of Co doping on structural and mechanical properties of CeO_2, in: AIP Confernce Proceddings 1966, 1966, AIP Conference Proceedings, 2018.

[39] K. Suzuki, M. Kato, T. Sunaoshi, H. Uno, U. Carvajal-Nunez, A.T. Nelson, K.J. McClellan, Thermal and mechanical properties of CeO_2, J. Am. Ceram. Soc. 102 (2019) 1994–2008.

[40] A.B. Shorey, K.M. Kwong, K.M. Johnson, S.D. Jacobs, Nanoindentation hardness of particles used in magnetorheological finishing (MRF), Appl. Opt. 39 (2000) 5194–5204.

[41] R.A. Wolfe, S.F. Kaufman "Mechanical properties of oxide fuels (LSBR/LWB development program)"

[42] A. Baena, T. Cardinaels, J.V. Eyken, J.L. Puzzolante, K. Binnemans, M. Verwerft, Effect of sintering atmosphere on the hardness of ThO_2, J. Nucl. Mater. 477 (2016) 222–227.

[43] S.M. Lang, F.P. Knudsen, Some physical properties of high density thorium dioxide, J. Am. Ceram. Soc. 39 (1956) 415–424.

[44] S. Spinner, L. Stone, F.P. Knudsen, Temperature dependence of the elastic constants of Thoria specimens of varying porosity, J. Res. Natl. Bur. Std. 67C (1963) 93–100.

[45] P.M. Macedo, W. Capps, J.O. Wachtman Jr., Elastic constants of single crystal of ThO_2 at 25°C, J. Am. Ceram. Soc. 47 (1964) 651.

[46] W.C. Oliver, G.M. Pharr, An improved technique for determining hardness and Young's modulus using load and displacement sensing indentation experiments, J. Mater. Res. 7 (1992) 1564–1583.

[47] J.M. Wheeler, D.E.J. Armstrong, W. Heinz, R. Schwaiger, High temperature nanoindentation: the state of the art and future challenges, Curr. Opin. Sol. Stat. Mater. Sci. 19 (2015) 354–366.

[48] Payan, T.J. Ulrich, P.Y. Le Bas, T. Saleh, M. Guimaraes, Quantitative linear and nonlinear resonance inspection techniques and analysis for material characterization: application to concrete thermal damage, J. Accoust. Soc. Am. 136 (2014) 537–546, doi:10.1121/1.4887451.

[49] A. Migliori, J.D. Maynard, Implementation of a modern resonant ultrasound spectroscopy system for the measurement of the elastic moduli of small solid specimens for the measurement of the elastic moduli of small solid specimens, Rev. Sci. Instrum. 76 (2005), doi:10.1063/1.2140494,121301-1-121301e7.

[50] J.T. White, A.T. Nelson, Thermal conductivity of UO_{2+x} and U_4O_{9-y}, J. Nucl. Mater. 443 (2013) 342–350.

[51] F.F. Balakirev, S.M. Ennaceur, R.J. Migliori, B. Maiorov, A. Migliori, Resonant ultrasound spectroscopy: the essential toolbox, Rev. Sci. Instrum. 90 (12) (2019) 14, doi:10.1063/1.5123165.

[52] J.A. Evans, B. Clausen, S.C. Vogel, F.F. Balakirev, J.B. Betts, L. Capolungo, R.A.B. Lebensohn, Maiorov "Determining elastic anisotropy of textured polycrystals using resonant ultrasound spectroscopy, J. Mater. Sci. 56 (2021) 10053–10073.

[53] B. Maiorov, J.B. Betts, P. Soderlind, A. Landa, S.C. Hernandez, T.A. Saleh, F.J. Freibert, A. Migliori, Elastic moduli of delta-Pu-239 reveal aging in real time, J. Appl. Phys. 121 (12) (2017) 9, doi:10.1063/1.4978509.

[54] E.S. Wood, J.T. White, A.T. Nelson, The effect of aluminum additions on the oxidation resistance of U_3Si_2, J. Nucl. Mater. 489 (2017) 84–90.

[55] S. Maskova, K. Miliyanchuk, L. Havela, Hydrogen absorption in U_3Si_2 and its impact on electronic properties, J. Nucl. Mater. 487 (2017) 418–423.

[56] E.S. Wood, J.T. White, C.J. Grote, A.T. Nelson, U_3Si_2 behavior in H_2O: part I, flowing steam and the effect of hydrogen, J. Nucl. Mater. 501 (2018) 404–412.

[57] J.M. Wheeler, J. Michler, Invited article: indenter materials for high temperature nanoindentation, Rev. Sci. Instr. 84 (2013) 101301.

[58] A.P. Shivprasad, D.M. Frazer, V.K. Mehta, M.W.D. Cooper, T.A. Saleh, J.T. White, J.R. Wermer, E.P. Luther, D.V. Rao, Elastic moduli of high-density, sintered monoliths of yttrium dihydride, J. Alloy Compd. 826 (2020) 153955.

[59] J.B. Wachtman, W.E. Tefft, D.G. Lam, C.S. Apstein, Exponential temperature dependence of Young's modulus for several Oxides, Phys. Rev. 122 (1961) 1754–1759.

[60] Y.P. Varshni, Temperature dependence of the elastic constants, Phys. Rev. B 2 (10) (1970) 3952–3958.

[61] G.M. Pharr, E.G. Herbert, Y. Gao, The indentation size effect: a critical examination of experimental observations and mechanistic interpretations, Annu. Rev. Mater. Res. 40 (2010) 271–292.

[62] R. McDonald, An Evaluation of the Mechanical Properties and Microstructure in Uranium Dioxide Doped with Oxide Additives, Thesis (2014).

[63] T.R.G. Kutty, T. Jarvis, C. Ganguly, Hot hardness and indentation creep studies on Zr-1Nb-1Sn-0.1Fe alloy, J. Nucl. Mater. 246 (2e3) (1997) 189e195.

[64] T.R.G. Kutty, K. Ravi, C. Ganguly, Studies on hot hardness of Zr and its alloys for nuclear reactors, J. Nucl. Mater. 265 (1e2) (1999) 91e99.

[65] U. Basak, A.K. Sengupta, C. Ganguly, Hot hardness and thermal conductivity of ThO_2-PuO_2 and ThO_2-UO_2 sintered pellets, J. Mater. Sci. Lett. 8 (4) (1989) 449e450.

[66] G. Sharma, R.V. Ramanujan, T.R.G. Kutty, G.P. Tiwari, Hot hardness and indentation creep studies of a Fe-28Al-3Cr-0.2C alloy, Mater. Sci. Eng. 278 (1e2) (2000) 106e112.

[67] E. Jossou, L. Malakkal, B. szpunar, D. Oladimeji, J.A. Szpunar, A first principles study of the electronic structure, elastic and thermal properties of UB_2, J. Nucl. Mater. 490 (2017) 41–48.

[68] L.J. Evitts, S.C. Middleburgh, E. Kardoulaki, I. Ipatova, M.J.D. Rushton, W.E. Lee, Influence of boron isotope ratio on the thermal conductivity of uranium diboride (UB_2) and zirconium diboride (ZrB_2), J. Nucl. Mater. 528 (2020) 151892.

[69] Tsui T.Y., Pharr G.M., Oliver W.C., Bhatia C.S., White R.L., Anders S., Anders A., Nanoindentation and nanoscratching of hard carbon coatings for magnetic discs, MRS Proceedings, Cambridge University Press, pp. 383-447.

[70] O.G. Brandt, C.T. Walker, Method for determining elastic constant changes, Rev. Sci. Instrum. 38 (6) (1967) 765-&, doi:10.1063/1.1720885.

[71] H.N. Yoshimura, A.L. Molisani, N.E. Narita, P.F. Cesar, H. Goldenstein, Porosity dependence of elastic constants in aluminum nitride ceramics, Mater. Res. 10 (2007).